Nanoscale Au@SiO_2-drug/VEGF as an *in vivo* probe for osteosarcoma diagnosis and therapy

TIANGUI CHEN*, TIANBO LI* and JIANGNING WANG

Department of Orthopedics Surgery, Beijing Shijitan Hospital, Capital Medical University, Beijing 100038, P.R. China

Received March 24, 2021; Accepted August 5, 2021

DOI: 10.3892/ol.2021.13027

Abstract. Osteosarcoma is a common primary bone malignancy, with a 5-year survival rate of only 20-30% in patients undergoing surgical treatment. Thus, it is important to identify novel methods for diagnosing and treating osteosarcoma, which was the aim of the present study. Vascular endothelial growth factor (VEGF) was used as the tumor-targeting protein to synthesize a multifunctional core-shell nanostructure, Au@SiO_2-drug/VEGF, in which the drug can be indocyanine green (ICG; as an optical tracer) or doxorubicin (DOX; as a chemotherapeutic agent). With VEGF as the osteosarcoma-targeting protein, Au exhibited optimal photothermal transformation performance, while SiO_2 served as the carrier for the drug. Au@SiO_2-ICG/VEGF nanoparticles (NPs) were evaluated for imaging and for the monitoring of drug accumulation in a tumor region in mice. Once the optimal drug accumulation was achieved, combined treatment of osteosarcoma (chemotherapy and photothermal therapy) was assessed. In the perioperative period associated with minimal invasive embolization of osteosarcoma, photothermal therapy and chemotherapy were applied for osteosarcoma diagnosis using Au@SiO_2-DOX/VEGF NPs. Taken together, the results of the present study provide a promising strategy for tumor detection prior to surgical treatment to improve the survival outcome of patients with osteosarcoma.

Introduction

Osteosarcoma is a common primary bone malignancy (1). Originating from mesenchymal tissue, osteosarcoma is the most prevalent bone tumor in childhood and adolescence and has high malignancy (1). The incidence of osteosarcoma is high, with a sex ratio of 3:2 (male to female), and the 5-year survival rate is only 20-30% in patients undergoing surgical treatment alone (2). Although chemotherapy extends the 5-year survival rate to 60-80%, ~50% of patients with osteosarcoma do not respond to chemotherapy (1). Locally, osteosarcoma exhibits aggressive growth and is prone to recurrence (3). Hematogenous metastasis to the lungs is the most common type of osteosarcoma metastasis, and the main cause of mortality is pulmonary metastasis (4). Early clinical symptoms primarily include local pain or swelling, related joint dysfunction, and in a small number of cases, pathological fractures (5). The majority of patients present with lung or systemic metastasis, low survival rate, and high mortality, and highly malignant osteosarcoma (unpublished data). However, the etiology and pathogenesis of osteosarcoma remain unclear (6). Clinically, it is important to improve the survival outcomes of patients with osteosarcoma and maintain limb function as much as possible to avoid the psychological trauma of amputation. Thus, it is critical to identify novel methods for diagnosing and treating osteosarcoma.

The growth and metastasis of a tumor are dependent on the formation of new blood vessels, and this process is under the joint control of oncogenic and tumor-suppressive factors of angiogenesis (7). Vascular endothelial growth factor (VEGF) is the most important stimulatory factor of tumor angiogenesis (8,9). Thus, its concentration can reflect the formation, progression and regression of tumors. Tumor growth and metastasis are rapid (7). During the transformation of a tumor cell mass into a solid tumor, tumor cells produce a large amount of VEGF to promote angiogenesis. At this point, the tumor is usually at an early stage, which is the best time for tumor screening, and can be diagnosed by existing clinical methods (8). Early screening can improve patient survival rate and prolong survival (9). A change in an angiogenesis trend is accompanied by a change in VEGF levels (8). Thus, VEGF can be employed for the screening of patients for almost any solid tumors, and its broad spectrum of specificity cannot be matched by other tumor indicators (10). In the clinic, several malignant tumors lack specific tumor markers, whereas VEGF has high sensitivity and broad specificity (11). An anomalous serum VEGF concentration can indicate the risk of a solid tumor (12). In addition, monitoring the level of VEGF regularly can help to determine the stage of tumor progression and to make an auxiliary judgment on the prognosis of the tumor (12). Thus, the higher the VEGF level, the higher the

Correspondence to: Professor Jiangning Wang, Department of Orthopedics Surgery, Beijing Shijitan Hospital, Capital Medical University, 10 Tieyi Street, Haidian, Beijing 100038, P.R. China
E-mail: wangjn@bjsjth.cn

*Contributed equally

Key words: osteosarcoma, diagnosis, therapy, targeting probe, vascular endothelial growth factor, *in vivo*

tumor malignancy and the worse the prognosis within the same tumor type. Generally, VEGF can be found at an early stage of cancer, and the detection of cancer at this stage greatly affects the survival rate and survival time of patients (12). VEGF is a broad-spectrum tumor marker suitable for the screening of several tumors (12) and can be combined with other tumor markers, thereby effectively improving the accuracy of cancer screening. The sensitivity of VEGF for tumor detection is high (better than that of traditional tumor markers), and the limit of detection of this assay is at the picogram level (12).

Photothermal therapy (PTT), an effective non-invasive treatment for different types of diseases, has been extensively investigated as a cancer treatment due to its unique low invasiveness, relatively simple administration and convenient direct heating in tumors (13-15). Several types of photosensitizers that strongly absorb near-infrared (NIR) light have been used as imaging agents (16). An example is indocyanine green (ICG), which is the only substance approved by the U.S. Food and Drug Administration (FDA) for NIR imaging that has been used clinically for retinal imaging and for evaluation of liver function, as well as for guiding biopsies (17,18). However, ICG has low photothermal conversion efficiency (16). Thus, there is an urgent requirement for materials with better photothermal conversion to replace ICG. Among the relevant nanoparticles (NPs), gold NPs (AuNPs) have been investigated due to their favorable biocompatibility and ability to convert NIR light into local heat (19). A combination of PTT and chemotherapy should greatly improve the clinical outcomes of osteosarcoma. The present study conjugated doxorubicin (DOX) with AuNPs to achieve combined photothermal and chemotherapeutic anticancer effects to inhibit the growth of the primary tumor and to suppress its metastasis.

Multifunctional core-shell nanostructures as a drug carrier were recently created to overcome the limitations of tumor imaging and therapy (20-23). Inorganic nanocrystals, such as those of Au and Ag, possess excellent heat conduction properties (19,24). In the process of ablation, the generated heat is rapidly transferred through inorganic crystals (AuNPs), which improve the heat transfer efficiency and contribute to the goal of killing tumor cells (23). Thus, there is an urgent requirement for in-depth investigation of suitability of AuNPs and other NPs for cancer cell imaging and therapy (25,26). Furthermore, researchers have proposed targeting nanocarriers that can be used for improving the stability of NPs or drugs and for targeted imaging (27,28), such as mesoporous silica, owing to its large surface area, large accessible pore volume and well-defined surface properties (28). As a shell (SiO_2 or $mSiO_2$), this substance may be widely used as a drug carrier to protect inorganic nanocrystals from aggregating (29-31). Thus, the present study investigated Au@SiO_2 as a core-shell nanocarrier for combined PTT and chemotherapy of osteosarcoma.

Given their unique applications in cancer imaging and therapy (32,33), a series of nanomaterials have been successfully developed, including polymeric NPs, quantum dots, and graphene, gold and magnetic nanomaterials. AuNPs possess several attractive features, such as low toxicity, biocompatibility, high chemical stability, and sonocatalytic properties (32,33). Core-shell nanostructures are an important way to protect NPs from aggregation (23). Therefore, mesoporous silica-coated Au nanorods (AuNP@SiO_2) have received much attention in the fields of PTT (34) and sonodynamic cancer therapy (35,36). However, there have been no reports on the application of AuNP@SiO_2 in osteosarcoma animal models for both imaging and therapy; such a study would be a critical step towards understanding how these materials behave *in vivo* for further clinical applications against osteosarcoma. Thus, the present study designed a probe composed of SiO_2-coated AuNPs incorporating ICG or DOX (Au@SiO_2_ICG or Au@SiO_2_DOX).

The present study investigated a multifunctional core-shell nanostructure composed of ICG/DOX-loaded SiO_2 (Au@SiO_2-drug/VEGF) for diagnosing osteosarcoma and for combined PTT and cytotoxic chemotherapy. Au@SiO_2-ICG/VEGF was used to determine tumor localization via fluorescence imaging (NIR) technology. Au@SiO_2-DOX/VEGF was used for the combined PTT and chemotherapy. The results demonstrated that targeted combination therapy is more effective against osteosarcoma compared with DOX chemotherapy alone. This technology can substantially contribute to the development and understanding of novel techniques for the detection of malignant tumors.

Materials and methods

Materials. Au@SiO_2 NPs were purchased from Hangzhou Xinqiao Biotechnology Co., Ltd., whereas ICG and DOX were purchased from the Alfa Aesar Company. DMEM, fetal bovine serum (FBS), penicillin-streptomycin, trypsin-EDTA and Hoechst were purchased from Gibco; Thermo Fisher Scientific, Inc. All other reagents used in the present study were purchased from Sinopharm Group Co., Ltd. and were of certified analytical reagent grade.

Synthesis of Au@SiO_2-drug and Au@SiO_2-drug/VEGF NPs. First, 0.5 ml of Au@SiO_2 solution was added into a flask and NaOH solution (100 μl; 0.1 M) was subsequently added. Tetraethyl orthosilicate (30 μl; 20% in methanol) was added at 30 min intervals. Either ICG (200 μl; 5 mg/ml) or DOX (200 μl; 5 mg/ml) were added to the solution. After 30 min, the final dose of tetraethyl orthosilicate was added and the mixture was subjected to a lucifugal reaction, which was allowed to proceed for 2 days in the dark at room temperature. The Au@SiO2-drug nanostructure was separated via centrifugation at 335.4 x g at room temperature and by decantation after the reaction. Finally, 10 mg/ml NH_2-polyethylene glycol (PEG)-VEGF (>3500 Da) was added to modify the surface of the NPs. The product, Au@SiO_2-drug/VEGF NPs, was stored at 4˚C.

Characterization. Transmission electron microscopy (TEM, HITACHI JEM-1011; Hitachi, Ltd.) and scanning electron microscopy (SEM, EM-30AX; COXEM Co., Ltd.) were performed to evaluate the morphology and size of Au@SiO_2-ICG NPs (in an aqueous dispersion) at 120 kV acceleration voltage. The hydrodynamic particle size distribution was determined on a Malvern Zetasizer (ZEN 3600; Malvern Instruments, Ltd.). Absorbance spectra of ICG and Au@SiO_2-ICG were recorded via ultraviolet-visible spectroscopy (UV-2450; Shimadzu Corporation), and fluorescence spectra were acquired on a fluorescence spectrofluorometer (F-7000; Hitachi, Ltd.), with excitation at wavelengths of 780 and 808 nm, respectively.

Photothermal effects in vitro. Aqueous solutions (1 ml) of free ICG (1 mg/ml), Au@SiO_2 (4 mg/ml) and Au@SiO_2-ICG (4 mg of Au@SiO_2 per 1 mg of ICG) were irradiated with an 808 nm continuous laser at a power density of 8 W/cm^2 for 7 min. The temperature was registered every minute by means of a Fluke infrared thermal imager (TI400; FLUKE). Each assay was repeated three times. As a control, 1 ml of PBS was irradiated to record the temperature at the same laser settings.

Cell culture. The human osteosarcoma cell line, MG63-Luc (Procell Life Science & Technology Co., Ltd.) was used for both *in vitro* and *in vivo* experiments. MG63-Luc cells express green fluorescent protein and firefly D-luciferin, and are compatible with a standard transfection protocol. Cells were cultured in Minimum Essential Medium supplemented with 10% FBS and 1% penicillin/streptomycin in a CO_2 incubator (Heracell) at 37˚C (36), according to the manufacturer's recommendations.

Cytotoxicity assessment. The cytotoxicity of Au@SiO_2-ICG and Au@SiO_2-ICG/VEGF NPs was assessed via the MTT assay, in the dark. MG63-Luc cells were seeded into 96-well plates at a density of $1x10^4$ cells/well and cultured for 24 h at 37˚C. Cells were incubated with different concentrations of the probe. Concentrations of Au@SiO_2-ICG and Au@SiO_2-ICG/VEGF NPs in 0, 6.25, 12.5, 25, 50, 100, 200, 300 and 400 μg/ml were assessed. The viability of the treated cells was determined via the MTT assay. Briefly, 10 μl of the MTT reagent (5 mg/ml) was added into each well and incubated for 4 h. DMSO was subsequently added to dissolve the formazan crystals and absorbance was measured at 570 nm wavelength using a microplate absorbance reader (Bio-Rad iMARK™; Bio-Red Laboratories, Inc.).

Animal experiments. A total of 20 BALB/c nude male mice (athymic, 5-weeks-old, ~20 g) were provided by Beijing Vital River Laboratory Animal Technology Co., Ltd. All animal experiments were approved by the Institutional Animal Care and Use Committee of the Capital Medical University (Beijing, China; approval no. CMU097230). Animal health and behavior were monitored every 2 days. The following housing conditions were applied: Temperature, 20˚C; humidity, 55%; air exchange frequency, 15/h; bedding was cleaned every 3 days; light/dark cycle, 12/12 h; mice had free access to food and water. A suspension of ~$1x10^6$ MG63-Luc cancer cells in 100 μl of phosphate buffer (0.01 mol/l; pH 7.2) was subcutaneously injected into the axillary fossa of each mouse to establish the subcutaneous tumor model. The tumors were allowed to grow for 2-3 weeks until a signal of a 0.8 cm diameter was detectable via *in vivo* Imaging System (IVIS). The tumor-bearing mice were injected with a probe (200 μl) for *in vivo* detection (n=5 for each imaging probe or dye). Each mouse was anesthetized with 2% isoflurane prior to IVIS imaging. Cervical dislocation was applied to all mice for euthanasia 25 days post-probe injection. The duration of the animal experiment (from injection to euthanasia) was ~50 days.

NIR fluorescence imaging in vivo. For *in vivo* fluorescence imaging, six subcutaneous osteosarcoma tumors were selected when the diameter of each tumor reached 5-6 mm. The mice were randomly divided into two groups (ICG and Au@SiO_2-ICG; n=3/group). Each mouse was anesthetized with 2% isoflurane. A solution of either free ICG or Au@SiO_2-ICG in 10 mM phosphate buffer pH 7.2 (150 μl) was injected into mice via the tail vein. The region of interest was examined after 10 min and 24, 48, 72 and 96 h using an IVIS Spectrum imaging system (PerkinElmer, Inc.), with an excitation wavelength of 745 nm and an emission wavelength of 840 nm. The data were analyzed using IVIS Living Imaging 3.0 software (PerkinElmer, Inc.).

Photothermal therapy in vivo. Mice bearing a tumor were injected with Au@SiO_2/VEGF in the tail vein and irradiated for 12 min post-injection under laser. Probe concentration was 2, 4, 6, 8 mg/ml under 1.4 W and 0, 1, 2, 4 mg/ml under 2 W. The irradiation-induced temperature rise was recorded by a Fluke infrared thermal imager.

Tumor xenografts and antitumor therapy. To determine the most appropriate laser power and probe concentration, the subcutaneous-tumor model mice were divided into different groups, receiving either PBS or different concentrations of probe prior to 1.4/2 W laser power PTT. Each mouse was anesthetized with 2% isoflurane prior to PTT. The laser irradiation time was limited to 5 min to avoid possible tissue damage by hyperthermia. The temperature and photothermal images of the tumor surface during the laser irradiation were recorded every minute via the infrared thermal imaging system. Once the optimal laser power and probe concentration were confirmed (1.4 W with 4 mg/ml), tumor bearing mice were treated with DOX (24 mg/kg) + 808 nm laser or Au@SiO_2-DOX/VEGF (injection volume, 200 μl and probe concentration, 4 mg/ml) + 808 nm laser to assess the effect of PTT combined with chemotherapy. Tumor size was measured using a vernier caliper, and body weight was measured every 5 days using an electronic balance. On day 25, the mice model was assessed using a small animal optical molecular imaging system (IVIS Spectrum imaging system; PerkinElmer, Inc.) and analyzed using IVIS Living Imaging 3.0 software (PerkinElmer, Inc.). The mice received 80 μl of D-Luciferin solution (15 mg/ml) via intraperitoneal injection 8 min before bioluminescence imaging was performed. During imaging, the mice were anesthetized with 2% isoflurane and placed in the supine position. The parameters for the bioluminescence imaging system were as follows: Binning 4 and exposure time 1 sec.

Statistical analysis. Statistical analysis was performed using GraphPad Prism 7.05 software (GraphPad Software, Inc.). All experiments were performed in triplicate and data are presented as the mean ± SD. One-way ANOVA was used to compare differences between two groups. $P<0.05$ was considered to indicate a statistically significant difference by t-test.

Results

Characterization of Au@SiO2-drug/VEGF. Characterization was performed via SEM and size measurement. SEM analysis demonstrated that Au@SiO2-drug/VEGF NPs were successfully synthesized. Au@SiO2-drug/VEGF NPs had a good shape and a uniform size of ~90 nm (Fig. 1A). TEM

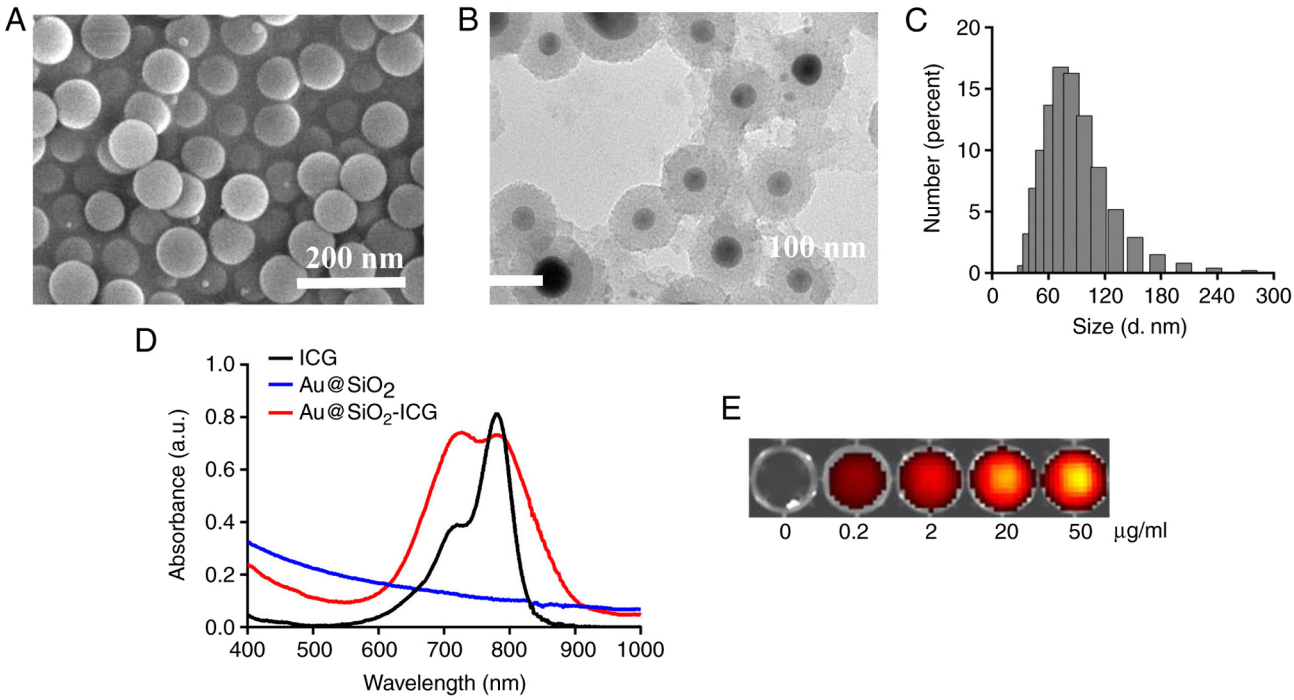

Figure 1. Characterization of Au@SiO_2-ICG/VEGF. (A) A scanning electron microscopy image of Au@SiO_2-ICG/VEGF NPs. (B) A transmission electron microscopy image of Au@SiO_2-ICG/VEGF NPs. (C) The hydrodynamic size of the nanocomposite particles was measured via dynamic light scattering. (D) The fluorescence imaging hysteresis loop of the Au@SiO_2-ICG/VEGF nanocomposite recorded at 300 K. (E) Fluorescence images of Au@SiO_2-ICG resuspended in water at different concentrations. ICG, indocyanine green; VEGF, vascular endothelial growth factor; NPs, nanoparticles; d., diameter.

analysis demonstrated homogeneous microstructure of the Au@SiO_2-drug/VEGF NPs, consistently with the SEM results (Fig. 1B). Hydrated-particle size was determined to verify the successful preparation of Au@SiO_2-drug/VEGF NPs. The size distribution was mainly in the range of 60-120 nm, and the average particle size of the bubbles was ~90 nm (Fig. 1C). Fig. 1D conveys that the absorption peak of free ICG was ~780 nm, while SiO_2 had no absorption peak. Notably, SiO_2 conjugated with ICG yielded two absorption peaks, at 700 and 780 nm. Furthermore, fluorescence intensity of the peak at 700 nm was stronger than that of free ICG, suggesting that Au@SiO_2-ICG exhibits better optical performance compared with free ICG did. Qualitative analyses of Au@SiO_2-ICG indicated that the fluorescence intensity increased in a dose-dependent manner (Fig. 1E).

Au@SiO_2-drug/VEGF in vivo biodistribution and the potential underlying mechanism. The expected cell-targeting mechanism was supported by the observed endocytosis of different NPs (Au@SiO_2-ICG/VEGF and Au@SiO_2-ICG) in the cancer cell line. This was confirmed via confocal fluorescence microscopy of MG63-Luc cells (Fig. 2A). There was an obvious difference in uptake between Au@SiO_2-ICG/VEGF and Au@SiO_2-ICG NPs (Fig. 2A). In the band of ICG, there were endocytosed Au@SiO_2-ICG/VEGF NPs and staining of the plasma membrane of MG63 cells. Furthermore, through quantification of cellular endocytosis of Au@SiO_2-ICG/VEGF and Au@SiO_2-ICG (200 mg/ml) via flow cytometry, NP uptake efficiency was determined in MG63 cells. A distinct change in the fluorescence intensity of Au@SiO_2-ICG/VEGF-fed MG63 cells in the fla-1 channel (563 nm) was observed (Fig. 2B). The results demonstrated that the VEGF protein had high efficiency of cancer cell targeting. To confirm that Au@SiO_2-ICG/VEGF and Au@SiO_2-ICG are biocompatible agents, biodistribution and toxicology assays at different concentrations (0, 6.25, 12.5, 25, 50, 100, 200, 300 and 400 μg/μl) were performed with irradiation via the MTT assay (Fig. 2C). The assays revealed notable decreases in cell viability at concentrations ranging from 0-400 μg/ml. Without a marked difference, Au@SiO_2-ICG/VEGF and Au@SiO_2-ICG yielded the same cell viability trends as ICG, which is approved by the FDA. Thus, Au@SiO_2-ICG/VEGF NPs appear to be a biocompatible and nontoxic agent for *in vivo* imaging use.

In vivo metabolism of the probe. Fluorescence imaging represents a non-invasive highly sensitive tissue distribution assay in real-time (18). Our method of fluorescence imaging (37) enabled highly sensitive real-time imaging of osteosarcoma to assess the metabolism of Au@SiO_2-ICG/VEGF and its accumulation by the subcutaneous tumor. The mice carried subcutaneous osteosarcoma tumors derived from MG63 cells. The Au@SiO_2-ICG/VEGF probe generated a strong fluorescence signal in the tumor region (Fig. 3) according to the IVIS Spectrum imaging system (PerkinElmer, Inc.), and the data were analyzed using IVIS Living Imaging 3.0 software (PerkinElmer, Inc.). Following fluorescence imaging *in vivo*, the mice were analyzed for fluorescence at 24 h post injection, and both prone and supine views of the NIR data were obtained (Fig. 3A). As presented in Fig. 3A, it is easy to see that the probe accumulated at the site of the subcutaneous tumor and outlined the tumor boundary. The probe was found to be metabolized by the liver and kidneys for 18 h. In addition, the present study quantitated the probe distribution *in vivo* in the whole-body tissue distribution analysis presented in Fig. 3A. The Au@SiO_2_ICG probe, which

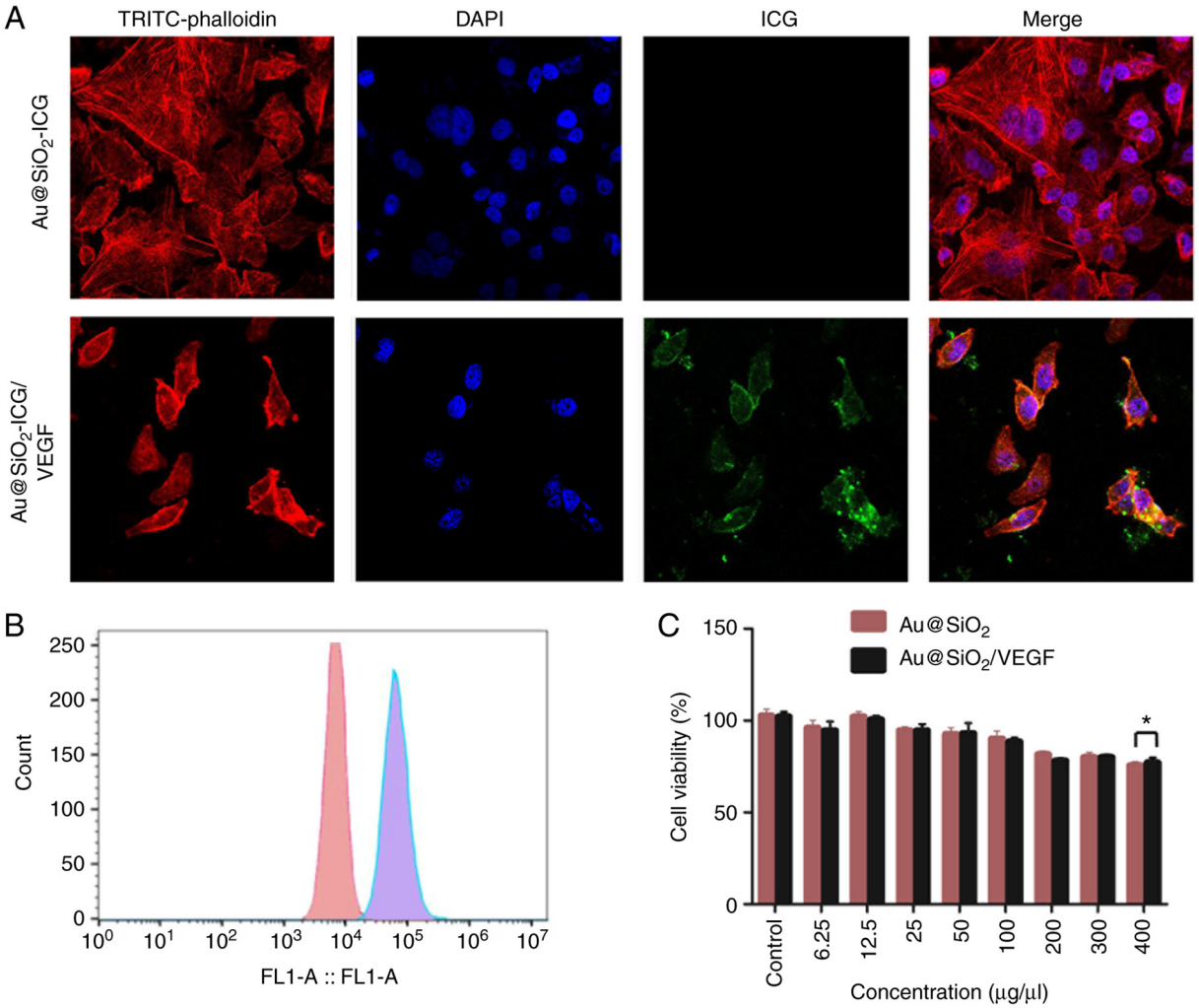

Figure 2. Cytotoxicity and endocytosis of Au@SiO2/VEGF NPs *in vitro*. (A) Confocal-microscopy images of Au@SiO2/VEGF taken up by MG63 cells. The cell nuclei were stained with DAPI (blue), actin was stained with TRITC-phalloidin (red), and Au@SiO2/VEGF NPs were visualized with near-infrared light (green). (B) Flow cytometric analysis of the uptake of Au@SiO_2-ICG/VEGF (purple) and Au@SiO_2-ICG (red) by MG63 cells. (C) The MTT assay was performed to assess cell viability at different concentrations of Au@SiO_2/VEGF NPs. *P<0.05. VEGF, vascular endothelial growth factor; NPs, nanoparticles; TRITC, tetramethylrhodamine; ICG, indocyanine green.

was found to be distributed uniformly throughout the whole body initially, was slowly metabolized over time (Fig. 3B). The time point corresponding to the optimal tumor accumulation of Au@SiO_2-ICG/VEGF *in vivo* was at 8 h, according to the tumor/background signal ratio (Fig. 3C).

Probe based PTT of osteosarcoma. To investigate the most appropriate laser power and probe concentration of Au@SiO_2/VEGF-based PTT *in vivo*, the photothermal effect of Au@SiO_2/VEGF was monitored using an infrared thermal imaging camera post 1.4/2 W laser power irradiation, with different probe concentrations. As the laser power increases, the temperature curve should also increase more rapidly, thus the concentration range assessed under 2 W is narrow compared with 1.4 W. The laser irradiation time was limited to 5 min to avoid possible tissue damage by hyperthermia. The mice were conscious, and the healthy epidermis was not burned during the laser irradiation. The temperature and photothermal images of the tumor surface during the laser irradiation were recorded every minute by the infrared thermal imaging system (Fig. 4A), and tumor temperature gradually increased with the time of laser radiation as recorded by thermal camera. A notable increase in tumor temperature was observed in Au@SiO_2/VEGF-injected mice, whereas the tumor temperature increase was minimal in mice injected with PBS (Fig. 4B). In addition, the temperature was higher and increased more rapidly following treatment with greater laser power and higher probe concentration. Furthermore, the temperature was higher as the probe concentration increased under the same laser power. A similar trend was observed when the laser power increased under the same probe concentration (Fig. 4B). According to a previous study (13), tumor cells are effectively eliminated at 42˚C, thus the present study selected 1.4 W laser power with 4 mg/ml probe concentration for subsequent experimentation. Images of mice treated with 1.4 W laser power and 4 mg/ml probe concentration were taken on days 0, 1 and 20. Tumor shrinkage was observed; however, tumor residual remained, thus a more effective strategy against osteosarcoma, such as combination therapy, is required.

Combined PTT and cytotoxic chemotherapy of osteosarcoma. Dual anticancer effects of Au@SiO_2-DOX/VEGF

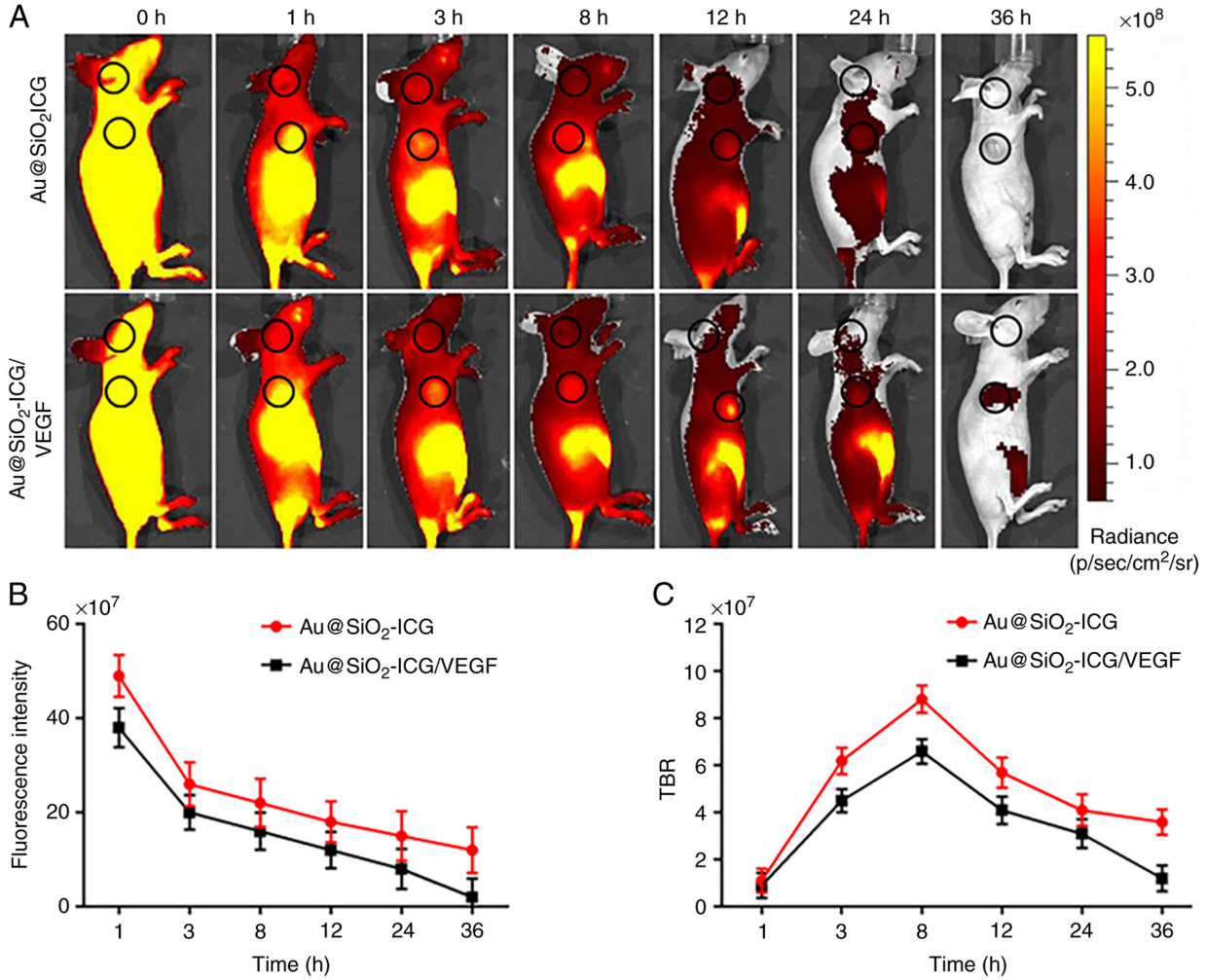

Figure 3. *In vivo* fluorescence images of subcutaneous-MG63-Luc-tumor-bearing mice in the prone position. (A) Images were captured at different time points after intravenous injection of Au@SiO_2/ICG/VEGF or Au@SiO_2/ICG NPs. Scale bar, 1 cm. Black circle near the upper limb indicates tumor region, while black circles on faces indicate the region selected to calculate background signal. (B) Quantitative analysis of probe distribution. (C) The TBR. TBR, tumor/background signal ratio; VEGF, vascular endothelial growth factor; ICG, indocyanine green; NPs, nanoparticles.

were assessed in tumor-bearing nude mice. Athymic nude mice (5-weeks-old) were subcutaneously injected with $2x10^6$ MG63-Luc cells into the dorsal right side. The tumor formed after 14 days, and its volume was calculated via multiplication of the largest and smallest dimensions. A total of 12 mice were randomly divided into two groups to assess the photothermal properties of Au@SiO_2-DOX/VEGF. Au@SiO_2-DOX/VEGF group (n=6) was treated with the 808 nm laser for 5 min at 1.4 W/cm^2 after injection of the probe, while DOX group (n=6) received DOX and 808 nm laser treatment for 5 min at 1.4 W/cm^2 (Fig. 5A). Across the 25 days, the tumors had disparate growth trends in both treatment groups, imaging of tumor region was taken at day 0, 10 and day 25 of both groups and tumor regrowth was detected by IVIS at day 25. A strong synergistic antitumor effect was achieved when combining PTT and chemotherapy, and the tumor growth in Au@SiO_2-DOX/VEGF group was almost completely inhibited on day 25 (upper row in Fig. 5A). Notably, both treatments caused major cellular damage in cancerous tissues but not in normal tissues. Regrowth of the tumor was detected in the DOX-treated tumor group start from day 10 (lower row in Fig. 5A). Furthermore, in contrast to the slow linear decline of tumor volume in the Au@SiO2-DOX/VEGF group, tumor volume in the DOX group manifested linear growth after 10 days of treatment (Fig. 5B). Body weight remained stable in the Au@SiO2-DOX/VEGF group after 15 days, suggesting that mice in this group responded well to treatment and exhibited improved quality of life, including greater food and water consumption. Conversely, body weight increased in the DOX group after 15 days, which was associated with rapid tumor growth (Fig. 5C). Taken together, these results suggest that Au@SiO_2-DOX/VEGF and the laser are a safer and more effective method of eliminating tumor cells compared with DOX alone.

Discussion

The present study successfully synthesized a nanoscale probe Au@SiO_2-drug/VEGF and proved that the probe can specifically bind to osteosarcoma cells. Notably, Au@SiO_2-drug/VEGF and DOX exhibited enhanced antitumor activity when combined with NIR laser irradiation compared with DOX plus laser treatment *in vivo*. The antitumor effect of Au@SiO_2-DOX/VEGF may be attributed to cell-targeting

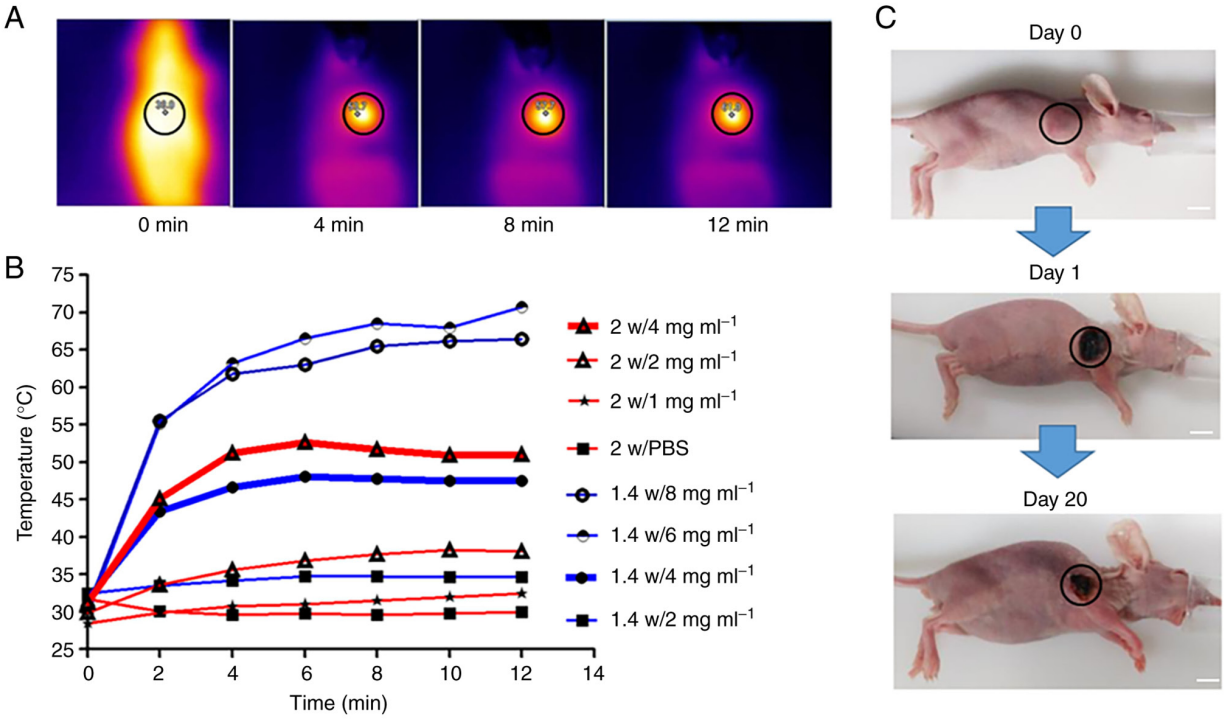

Figure 4. Thermal images of mice with subcutaneous tumors after intravenous injection of the probe (4 mg/ml; 200 μl) subjected to photothermal therapy under the 808 nm laser, with an output power of 1.4 W. (A) Temperature variation at different concentrations and laser power levels at various time points. (B) Quantitative analysis of temperature variation. (C) Images of treated mice. Black circles indicate tumor regions. Scale bar, 1 cm.

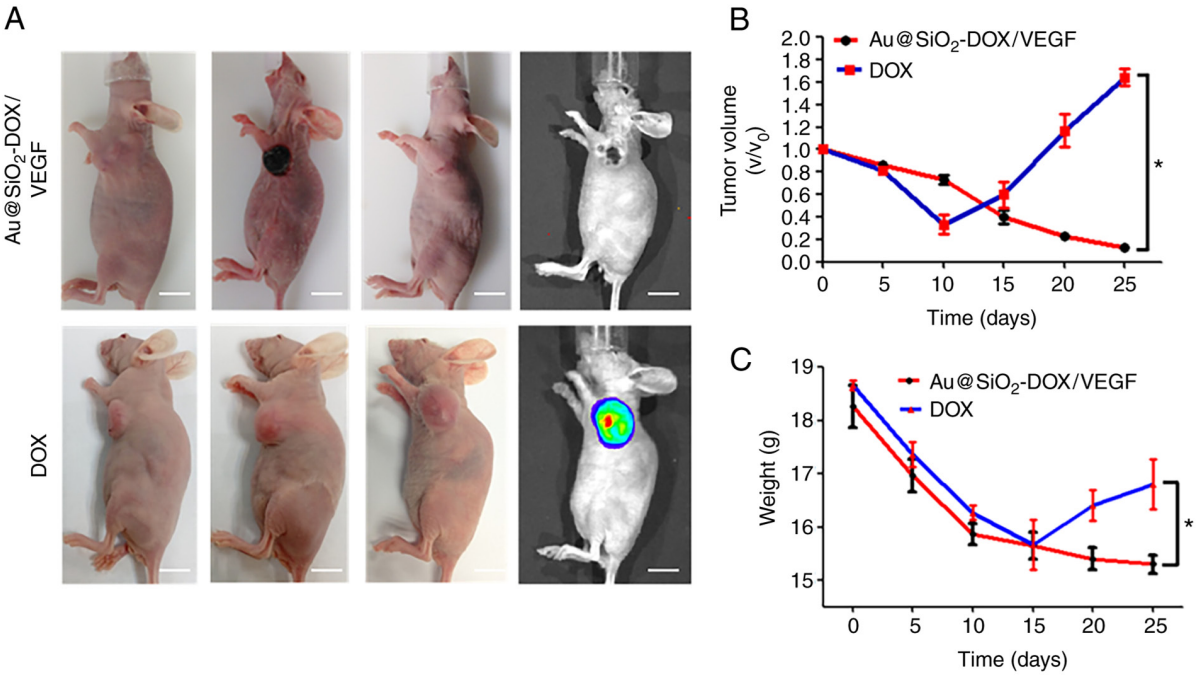

Figure 5. Performance of *in vivo* PTT and cytotoxic chemotherapy. (A) The effect of combination therapy on subcutaneous osteosarcoma tumor after injection of a drug (either Au@SiO2/DOX/VEGF or DOX). Images on the first column were taken prior to PTT, while images on the second column were taken following PTT. Images on the third column were taken on day 25, while images on the fourth column were taken via IVIS on day 25. Scale bar, 1 cm. (B) *In vivo* tumor volumes in mice treated with either Au@SiO_2-DOX/VEGF or DOX for 25 days. (C) Body weight of osteosarcoma-bearing mice treated with either Au@SiO_2-DOX/VEGF or DOX for 25 days. *P<0.05. PTT, photothermal therapy; DOX, doxorubicin; VEGF, vascular endothelial growth factor; IVIS, *in vivo* Imaging System.

endocytosis of the probe and the synergistic interaction between chemotherapy and PTT (22). In this nanoconstruct, VEGF peptide with high tumor binding affinity and high plasma stability was conjugated to Au@SiO_2 via a PEG linker, which ensured availability of the peptide to the target receptor. This strategy has been successfully used for the formulation

of other targeted NPs (38-41). Characterization of probe demonstrated that the probe NPs had a good nanosphere shape and a uniform size of ~90 nm. The probe exhibited optimal performance compared with free ICG, suggesting that the NP can potentially be used for tumor *in vivo* detection.

Both *in vitro* and *in vivo* data demonstrated that Au@SiO_2-drug/VEGF can be cell-targeting endocytosed. *In vivo*, Au@SiO_2-drug/VEGF displayed significantly higher accumulation compared with nontargeted Au@SiO_2-drug/VEGF in human osteosarcoma cells. Thus, the results of the present study support successful VEGF receptor-mediated targeted delivery of Au@SiO_2-drug/VEGF after intravenous injection. In addition to active targeting mediated by receptor ligands exemplified in the present study, physiological and physical methods, such as tumor priming, vascular disruption, degradation of the extracellular matrix and vessel normalization may be used to improve tumor distribution of NPs (42,43). These studies suggest that targeted NPs, such as Au@SiO_2-drug/VEGF, may achieve further improvement in tumor deposition when combined with physiological and physical methods.

The temperature of tumors in mice that received intravenous injection of probe reached ~47˚C after 5 min of continuous wave NIR laser exposure at 1.4 W/cm^2. This temperature is sufficient for inducing irreversible damage to cancer cells (44). In the present study, 1.4 W increased the temperature only when probe concentration was higher than 2 W. Au in the probe is known to have good photothermal conversion performance (44). The higher the probe concentration, the more Au and more heat generated (45,46). As expected, there was no temperature change in the tumors of mice that receives PBS injection followed by NIR irradiation. Therefore, Au@SiO_2-drug/VEGF mediates efficient photothermal effects. Among the different types of inorganic NPs, gold NPs are the most widely used for drug delivery and other biological applications, due to their non-toxic and biocompatible properties, their size- and shape-controllable synthesis, the ease of surface modification with functional thiolate ligands and their extremely rich and versatile optical heterogeneous and peculiar nature of individual cancers and the inability to target therapeutics to cancer cells without damaging normal tissues (43). There are studies using various nanostructures to medicate PTT, such as nanorod, nanoshell capsules and nancages (46-48), excellent photothermic conversion and promising antitumor activity have been observed. However, further studies are required to identify other nanostructured particles for the treatment of osteosarcoma.

The antitumor efficacy of Au@SiO_2-DOX/VEGF plus laser and free DOX plus laser was investigated in a 25-day follow up. The follow-up did not continue pass this point as the mice receiving free DOX plus laser has significantly weight loss and tumor size growth on day 25. The results demonstrated that mice receiving Au@SiO_2-DOX/VEGF plus laser had a significantly better prognosis. Thus, PTT and cell toxicity combined therapy may be a more effective therapy module compared with chemotherapy alone. In addition, a previous study reported that NP loaded cytotoxicity drug can reduce the side effects of chemotherapy due to controlled release (49). Osteosarcomas are deep-seated, bone tumors and their metastasis is associated with the lungs, which are deep-seated organs (1), so the clinical application of probe-based PTT for osteosarcomas may be tumor residual elimination following tumor resection. However, laser radiation before any incision is made considering the penetration of laser in human tissues.

In conclusion, the present study successfully developed Au@SiO_2-drug/VEGF NPs enabling simultaneous NIR hyperthermia and drug delivery. The Au@SiO_2-drug/VEGF NPs exhibited optimal antitumor efficacy and satisfactory biocompatibility. In addition, Au@SiO_2-drug/VEGF exhibited good targeting performance towards osteosarcoma due to the targeting agent, VEGF. It was confirmed that the combined treatment (cytotoxic chemotherapy and PTT) can be administered to mice and successfully suppress the cancer and prolong the survival time. Taken together, these results suggest that Au@SiO_2-drug/VEGF delivers targeted heating and drugs to tumor tissues and minimizes collateral damage to healthy tissues. Thus, this approach has great potential for effective treatment of different types of tumors. Given that this therapy is both feasible and effective, it may be incorporated into clinical practice in the near future.

Acknowledgements

Not applicable.

Funding

The present study was funded by the National Nature Science Foundation of China (grant no. 81473502).

Availability of data and materials

The datasets used and/or analyzed during the current study are available from the corresponding author on reasonable request.

Authors' contributions

TC and TL made substantial contributions to conception and design, acquisition of data and analysis and interpretation of data. TC was involved in drafting the manuscript and revising it critically for important intellectual content. JW made substantial contributions to conception and design and gave final approval of the version to be published. TC and JW confirm the authenticity of all the raw data. All authors read and approved the final manuscript.

Ethics approval and consent to participate

All animal experiments were approved by the Institutional Animal Care and Use Committee of the Capital Medical University (Beijing, China; approval no. CMU097230).

Patient consent for publication

Not applicable.

Competing interests

The authors declare that they have no competing interests.

References

1. Isakoff MS, Bielack SS, Meltzer P and Gorlick R: Osteosarcoma: Current treatment and a collaborative pathway to success. J Clin Oncol 33: 3029-3035, 2015.
2. Bramwell VH, Burgers M, Sneath R, Souhami R, van Oosterom AT, Voûte PA, Rouesse J, Spooner D, Craft AW, Somers R, *et al*: A comparison of two short intensive adjuvant chemotherapy regimens in operable osteosarcoma of limbs in children and young adults: The first study of the European Osteosarcoma Intergroup. J Clin Oncol 10: 1579-1591, 1992.
3. Roberts RD, Lizardo MM, Reed DR, Hingorani P, Glover J, Allen-Rhoades W, Fan T, Khanna C, Sweet-Cordero EA, Cash T, *et al*: Provocative questions in osteosarcoma basic and translational biology: A report from the Children's Oncology Group. Cancer 125: 3514-3525, 2019.
4. Fauske L, Lorem G, Grov EK and Bondevik H: Changes in the body image of bone sarcoma survivors following surgical treatment-A qualitative study. J Surg Oncol 113: 229-234, 2016.
5. Guerra RB, Tostes MD, da Costa Miranda L, Pires de Camargo O, Baptista AM, Caiero MT, Dos Santos Machado TM, Abadi MD, Mendes de Oliveira CR and Filippi RZ: Comparative analysis between osteosarcoma and Ewing's sarcoma: Evaluation of the time from onset of signs and symptoms until diagnosis. Clinics (Sao Paulo) 61: 99-106, 2006.
6. Wang D, Niu X, Wang Z, Song CL, Huang Z, Chen KN, Duan J, Bai H, Xu J, Zhao J, *et al*: Multiregion sequencing reveals the genetic heterogeneity and evolutionary history of osteosarcoma and matched pulmonary metastases. Cancer Res 79: 7-20, 2019.
7. Yang Y, Tian W, Yang L, Zhang Q, Zhu M, Liu Y, Li J, Yang L, Liu J, Shen Y and Qi Z: Gemcitabine potentiates anti-tumor effect of resveratrol on pancreatic cancer via down-regulation of VEGF-B. J Cancer Res Clin Oncol 147: 93-103, 2021.
8. Scarpellino G, Munaron L, Cantelmo AR and Fiorio Pla A: Calcium-permeable channels in tumor vascularization: Peculiar sensors of microenvironmental chemical and physical cues. Rev Physiol Biochem Pharmacol: Aug 19, 2020 (Epub ahead of print). doi: 10.1007/112_2020_32.
9. Yu C, Dou T, Liu Y and Liu R: Clinical value of TV-CDS combined with serum tumor markers in diagnosis of ovarian cancer. Oncol Lett 20: 2028-2034, 2020.
10. Mu L, Guan B, Tian J, Li X, Long Q, Wang M, Wang W, She J, Li X, Wu D and Du Y: MicroRNA-218 inhibits tumor angiogenesis of human renal cell carcinoma by targeting GAB2. Oncol Rep 44: 1961-1970, 2020.
11. Sanhueza C, Bennett JC, Valenzuela-Valderrama M, Contreras P, Lobos-González L, Campos A, Wehinger S, Lladser Á, Kiessling R, Leyton L and Quest AFG: Caveolin-1-mediated tumor suppression is linked to reduced HIF1α S-nitrosylation and transcriptional activity in hypoxia. Cancers (Basel) 12: 2349, 2020.
12. Apte RS, Chen DS and Ferrara N: VEGF in signaling and disease: Beyond discovery and development. Cell 176: 1248-1264, 2019.
13. Chen Q, Hu Q, Dukhovlinova E, Chen G, Ahn S, Wang C, Ogunnaike EA, Ligler FS, Dotti G and Gu Z: Photothermal therapy promotes tumor infiltration and antitumor activity of CAR T cells. Adv Mater 31: e1900192, 2019.
14. Lin X, Fang Y, Tao Z, Gao X, Wang T, Zhao M, Wang S and Liu Y: Tumor-microenvironment-induced All-in-One nanoplatform for multimodal imaging-guided chemical and photothermal therapy of cancer. ACS Appl Mater Interfaces 11: 25043-25053, 2019.
15. Wang Z, Zhen X, Upputuri PK, Jiang Y, Lau J, Pramanik M, Pu K and Xing B: Redox-activatable and Acid-enhanced nanotheranostics for second Near-infrared photoacoustic tomography and combined photothermal tumor therapy. ACS Nano 13: 5816-5825, 2019.
16. Feng Z, Yu X, Jiang M, Zhu L, Zhang Y, Yang W, Xi W, Li G and Qian J: Excretable IR-820 for in vivo NIR-II fluorescence cerebrovascular imaging and photothermal therapy of subcutaneous tumor. Theranostics 9: 5706-5719, 2019.
17. Bramos A, Perrault D, Yang S, Jung E, Hong YK and Wong AK: Prevention of postsurgical lymphedema by 9-cis retinoic acid. Ann Surg 264: 353-361, 2016.
18. Ogawa M, Kosaka N, Choyke PL and Kobayashi H: In vivo molecular imaging of cancer with a quenching near-infrared fluorescent probe using conjugates of monoclonal antibodies and indocyanine green. Cancer Res 69: 1268-1272, 2009.
19. Zhang F, Han X, Hu Y, Wang S, Liu S, Pan X, Wang H, Ma J, Wang W, Li S, *et al*: Interventional photothermal therapy enhanced brachytherapy: A new strategy to fight deep pancreatic cancer. Adv Sci (Weinh) 6: 1801507, 2019.
20. Mickoleit F, Lanzloth C and Schuler D: A versatile toolkit for controllable and highly selective multifunctionalization of bacterial magnetic nanoparticles. Small 16: e1906922, 2020.
21. Sun Z, Cheng K, Yao Y, Wu F, Fung J, Chen H, Ma X, Tu Y, Xing L, Xia L and Cheng Z: Controlled Nano-bio interface of functional nanoprobes for in vivo monitoring enzyme activity in tumors. ACS Nano 13: 1153-1167, 2019.
22. Kim KS, Han JH, Park JH, Kim HK, Choi SH, Kim GR, Song H, An HJ, Han DK, Park W and Park KS: Multifunctional nanoparticles for genetic engineering and bioimaging of natural killer (NK) cell therapeutics. Biomaterials 221: 119418, 2019.
23. Shang W, Zeng C, Du Y, Hui H, Liang X, Chi C, Wang K, Wang Z and Tian J: Core-shell gold Nanorod@Metal-Organic framework nanoprobes for multimodality diagnosis of glioma. Adv Mater: Nov 18, 2016 (Epub ahead of print). doi: 10.1002/adma.201604381.
24. Zhu P, Gao S, Lin H, Lu X, Yang B, Zhang L, Chen Y and Shi J: Inorganic nanoshell-stabilized liquid metal for targeted photonanomedicine in NIR-II biowindow. Nano Lett 19: 2128-2137, 2019.
25. Imani R, Dillert R, Bahnemann DW, Pazoki M, Apih T, Kononenko V, Repar N, Kralj-Iglič V, Boschloo G, Drobne D, *et al*: Multifunctional Gadolinium-doped mesoporous TiO2 nanobeads: Photoluminescence, enhanced spin relaxation, and reactive oxygen species photogeneration, beneficial for cancer diagnosis and treatment. Small: Apr 4, 2017 (Epub ahead of print). doi: 10.1002/smll.201700349.
26. Kumar A, Huo S, Zhang X, Liu J, Tan A, Li S, Jin S, Xue X, Zhao Y, Ji T, *et al*: Neuropilin-1-targeted gold nanoparticles enhance therapeutic efficacy of platinum(IV) drug for prostate cancer treatment. ACS Nano 8: 4205-4220, 2014.
27. Deng X, Liang S, Cai X, Huang S, Cheng Z, Shi Y, Pang M, Ma P and Lin J: Yolk-shell structured au Nanostar@Metal-Organic framework for synergistic chemo-photothermal therapy in the second Near-infrared window. Nano Lett 19: 6772-6780, 2019.
28. Gao J, Wang F, Wang S, Liu L, Liu K, Ye Y, Wang Z, Wang H, Chen B, Jiang J, *et al*: Hyperthermia-triggered On-demand biomimetic nanocarriers for synergetic photothermal and chemotherapy. Adv Sci 7: 1903642, 2020.
29. Peng D, Du Y, Shi Y, Mao D, Jia X, Li H, Zhu Y, Wang K and Tian J: Precise diagnosis in different scenarios using photoacoustic and fluorescence imaging with dual-modality nanoparticles. Nanoscale 8: 14480-14488, 2016.
30. Abbasi Pour S and Shaterian HR: Design and characterization of lisinopril-loaded superparamagnetic nanoparticles as a new contrast agent for in vitro, in vivo MRI imaging, diagnose the tumors and drug delivery system. J Mater Sci Mater Med 28: 91, 2017.
31. Liu P, Wang Y, Liu Y, Tan F, Li J and Li N: S-nitrosothiols loaded mini-sized Au@silica nanorod elicits collagen depletion and mitochondrial damage in solid tumor treatment. Theranostics 10: 6774-6789, 2020.
32. Wang Y, Huang Q, He X, Chen H, Zou Y, Li Y, Lin K, Cai X, Xiao J, Zhang Q and Cheng Y: Multifunctional melanin-like nanoparticles for bone-targeted chemo-photothermal therapy of malignant bone tumors and osteolysis. Biomaterials 183: 10-19, 2018.
33. Han HS, Choi KY, Lee H, Lee M, An JY, Shin S, Kwon S, Lee DS and Park JH: Gold-nanoclustered hyaluronan Nano-assemblies for photothermally maneuvered photodynamic tumor ablation. ACS Nano 10: 10858-10868, 2016.
34. Jin R, Yang J, Zhao D, Hou X, Li C, Chen W, Zhao Y, Yin Z and Liu B: Hollow gold nanoshells-incorporated injectable genetically engineered hydrogel for sustained chemo-photothermal therapy of tumor. J Nanobiotechnology 17: 99, 2019.
35. Deepagan VG, You DG, Um W, Ko H, Kwon S, Choi KY, Yi GR, Lee JY, Lee DS, Kim K, *et al*: Long-circulating Au-TiO_2 nanocomposite as a sonosensitizer for ROS-mediated eradication of cancer. Nano Lett 16: 6257-6264, 2016.
36. Lin X, Liu S, Zhang X, Zhu R, Chen S, Chen X, Song J and Yang H: An ultrasound activated vesicle of janus Au-MnO nanoparticles for promoted tumor penetration and sono-chemodynamic therapy of orthotopic liver cancer. Angew Chem Int Ed Engl 59: 1682-1688, 2020.
37. Deng H, Shang W, Lu G, Guo P, Ai T, Fang C and Tian J: Targeted and multifunctional technology for identification between hepatocellular carcinoma and liver cirrhosis. ACS Appl Mater Interfaces 11: 14526-14537, 2019.

38. Du Y, Liu X, Liang Q, Liang XJ and Tian J: Optimization and design of magnetic ferrite nanoparticles with uniform tumor distribution for highly sensitive MRI/MPI performance and improved magnetic hyperthermia therapy. Nano Lett 19: 3618-3626, 2019.
39. Davis ME, Zuckerman JE, Choi CH, Seligson D, Tolcher A, Alabi CA, Yen Y, Heidel JD and Ribas A: Evidence of RNAi in humans from systemically administered siRNA via targeted nanoparticles. Nature 464: 1067-1070, 2010.
40. Petros RA and DeSimone JM: Strategies in the design of nanoparticles for therapeutic applications. Nat Rev Drug Disco 9: 615-627, 2010.
41. Lu W, Zhang G, Zhang R, Flores LG II, Huang Q, Gelovani JG and Li C: Tumor site-specific silencing of NF-kappaB p65 by targeted hollow gold nanosphere-mediated photothermal transfection. Cancer Res 70: 3177-3188, 2010.
42. Lu D, Wientjes MG, Lu Z and Au JL: Tumor priming enhances delivery and efficacy of nanomedicines. J Pharmacol Exp Ther 322: 80-88, 2007.
43. Melancon MP, Elliott A, Ji X, Shetty A, Yang Z, Tian M, Taylor B, Stafford RJ and Li C: Theranostics with multifunctional magnetic gold nanoshells: Photothermal therapy and t2* magnetic resonance imaging. Invest Radiol 46: 132-140, 2011.
44. Zhu X, Feng W, Chang J, Tan YW, Li J, Chen M, Sun Y and Li F: Temperature-feedback upconversion nanocomposite for accurate photothermal therapy at facile temperature. Nat Commun 7: 10437, 2016.
45. Sanna V and Sechi M: Nanoparticle therapeutics for prostate cancer treatment. Nanomedicine 1 (Suppl 1): S31-S36, 2012.
46. Liao J, Li W, Peng J, Yang Q, Li H, Wei Y, Zhang X and Qian Z: Combined cancer photothermal-chemotherapy based on doxorubicin/gold nanorod-loaded polymersomes. Theranostics 5: 345-356, 2015.
47. Wang H, Zhao R, Li Y, Liu H, Li F, Zhao Y and Nie G: Aspect ratios of gold nanoshell capsules mediated melanoma ablation by synergistic photothermal therapy and chemotherapy. Nanomedicine 12: 439-448, 2016.
48. Dong L, Li Y, Li Z, Xu N, Liu P, Du H, Zhang Y, Huang Y, Zhu J, Ren G, *et al*: Au Nanocage-strengthed dissolving microneedles for chemo-photothermal combined therapy of superficial skin tumors. ACS Appl Mater Interfaces 10: 9247-9256, 2018.
49. You J, Zhang R, Xiong C, Zhong M, Melancon M, Gupta S, Nick AM, Sood AK and Li C: Effective photothermal chemotherapy using doxorubicin-loaded gold nanospheres that target EphB4 receptors in tumors. Cancer Res 72: 4777-4786, 2012.